Journal of Structural Geology 203 (2026) 105591

Contents lists available at ScienceDirect

Journal of Structural Geology

journal homepage: www.elsevier.com/locate/jsg

Dehydroxylation and amorphization of wet serpentinite gouges during experimental seismic slip and implications for coseismic fluid drainage

Li-Wei Kuo [a,b,c,d,*], Wei-Hsin Wu [e], Matthew S. Tarling [f], Steven A.F. Smith [g], Thi Trinh Nguyen [a], Wen-Jie Wu [h], Jialiang Si [i]

[a] Department of Earth Sciences, National Central University, 32001, Taoyuan, Taiwan
[b] Earthquake-Disaster & Risk Evaluation and Management (E-DREaM) Center, National Central University, 32001, Taoyuan, Taiwan
[c] Graduate Institute of Applied Geology, National Central University, 32001, Taoyuan, Taiwan
[d] Institute of Earth Sciences, Academia Sinica, 115201, Taipei, Taiwan
[e] Department of Geosciences, University of Padua, Padua, Italy
[f] Department of Earth, Ocean and Atmospheric Sciences, University of British Columbia, Vancouver, Canada
[g] GeoSmith Editing, 249 Strada Cantonale, Casaccia, 7602, Switzerland
[h] Department of Geology, Chinese Culture University, 11114, Taipei City, Taiwan
[i] Key Laboratory of Deep-Earth Dynamics of Ministry of Natural Resources, Institute of Geology, Chinese Academy of Geological Sciences, Beijing, China

A B S T R A C T

Dehydroxylation and amorphization of serpentinite occur in natural fault zones and laboratory experiments due to frictional heating during high-velocity slip. Although these processes have been demonstrated under relatively dry experimental conditions, it is unclear whether they are triggered in the presence of water. To address this, we performed rotary-shear friction experiments on water-saturated serpentinite powders at a slip rate of 1 m/s and a normal stress of 10 MPa, in both fluid-drained and undrained conditions. In all experiments, the apparent friction coefficient (i.e., shear stress divided by normal stress) decreased from a peak value of ~0.32–0.42 to a steady-state value of ~0.09–0.29. Undrained experiments were associated with gouge compaction, and the temperature measured by a thermocouple in the slip zone reached ~180 °C by the end of the experiments. Fluid-drained experiments were associated with both gouge compaction and dilation, and the maximum temperature reached ~635 °C. Using a combination of scanning electron microscopy, focused ion beam transmission electron microscopy, and synchrotron X-ray diffraction analysis, we demonstrate that dehydroxylation and amorphization of serpentinite to form nanocrystalline olivine and enstatite only occurs in fluid-drained conditions. One-dimensional numerical modeling accounting for the main phase changes (water to vapor and serpentine to olivine) shows that the temperature increases rapidly in both the undrained and drained experiments. However, fluid drainage progressively reduces the efficiency of thermal pressurization, leading to increased shear heating and the onset of dehydroxylation and amorphization under fluid-drained conditions. Our results suggest that the distinctive nanocrystalline products of dehydroxylation and amorphization reactions in natural fault zones can only form if fluid drainage occurs away from the slip zone during coseismic slip.

1. Introduction

Serpentinite occurs in a range of important tectonic settings, such as subduction zones (Bostock et al., 2002; Hyndman and Peacock, 2003; Reynard, 2013), oceanic detachment faults (Cann et al., 1997; Bach et al., 2006), and continental transform faults (Hekinian et al., 1992; Moore and Rymer, 2012; Barth et al., 2013). In these settings, serpentinite-bearing faults and shear zones, and the physical and chemical processes that occur along them during the seismic cycle, are likely to play a primary role in the rheology and strength of the lithosphere. Therefore, investigating the structure and composition of serpentinite-bearing shear zones is crucial to understanding crustal deformation during the seismic cycle.

Serpentinite shear zones often exhibit block-in-matrix fabrics, comprising a pervasively foliated matrix, incrementally developed slickenfibres and veins, and fractured or faulted phacoids that are embedded within the matrix (Collettini et al., 2011; Cowan, 1985; Cowan, 1990; Fagereng and Sibson, 2010; Festa et al., 2010; Kimura et al., 2012; Meneghini et al., 2009; Tarling et al., 2019a, 2022; Smith et al., 2024; Viti et al., 2018). The development of foliation is commonly interpreted as resulting from pressure-solution processes, which some authors have related to fault creep (Andréani et al., 2005). However, multi-generational vein networks within the foliated matrix and the phacoids suggest that hydrofracturing can occur throughout the shear zone (Fagereng et al., 2010; Ujiie et al., 2018), which may reflect elevated fluid pressures generated during syn-kinematic metasomatic

* Corresponding author. Department of Earth Sciences, National Central University, 32001, Taoyuan, Taiwan.
E-mail address: liweikuo@ncu.edu.tw (L.-W. Kuo).

https://doi.org/10.1016/j.jsg.2025.105591
Received 7 May 2025; Received in revised form 17 November 2025; Accepted 18 November 2025
Available online 22 November 2025
0191-8141/© 2025 Elsevier Ltd. All rights are reserved, including those for text and data mining, AI training, and similar technologies.

reactions (Tarling et al., 2019b, 2022). The discovery of nanocrystalline olivine and enstatite within the Livingstone Fault in New Zealand has been interpreted as reflecting the high-temperature dehydroxylation of serpentinite during coseismic rupture (Tarling et al., 2018). Integrating such geological observations with geophysical measurements (Peacock et al., 2011), numerical modeling (Maurer and Johnson, 2014), and laboratory experiments (Kohli et al., 2011; Tesei et al., 2018; Brantut et al., 2016) suggests that serpentinite-bearing shear zones can host both stable creep and unstable earthquake rupture.

Hirose and Bystricky (2007) conducted rotary-shear friction experiments on cohesive serpentinite samples at room humidity, slip velocities of 1.1 m/s, and normal stresses up to 24.5 MPa. They interpreted the observed dynamic weakening as resulting from flash heating and weakening of asperities on the experimental fault surfaces.Viti and Hirose (2009) and Viti and Hirose (2010) later characterized the products that formed during the experiments of Hirose and Bystricky (2007), identifying nanocrystalline forsterite, enstatite, and magnetite within the principal slip zones (PSZ), where most of the strain is accommodated during slip. Viti and Hirose (2010) inferred that temperatures of ~820–1200 °C were achieved within the PSZ during the experiments. Proctor et al. (2014) conducted rotary-shear experiments on both cohesive serpentinites and incohesive serpentinite gouges at a velocity of 1.1 m/s under room-humidity conditions. They reported similar dynamic weakening and identified olivine and enstatite within the PSZ of both the cohesive and incohesive samples. They suggested that dynamic weakening of serpentinites during seismic slip may be accompanied by dehydroxylation and possible melting, resulting in the formation of olivine and enstatite. Brantut et al. (2016) used a triaxial deformation apparatus at confining pressures of 30 and 95 MPa to trigger stick-slip events in samples of cohesive antigorite. They demonstrated that amorphization and possible melting of serpentinite occurred during sub-millimeter slip events and that these events were associated with near-zero dynamic friction values. Overall, these experimental studies, conducted under relatively dry conditions, indicate that the extreme dynamic weakening of both cohesive and incohesive serpentinites at high slip velocities is accompanied by dehydroxylation and the formation of nanocrystalline olivine and enstatite, as well as possible melting and formation of amorphous materials. Where these reaction products can be identified in natural fault zones, they serve as critical indicators of past seismic activity (Tarling et al., 2018).

Despite the above conclusions, it remains unclear whether dehydroxylation and amorphization of serpentinite are significant processes in the presence of water. To address this, we used a purpose-built gouge sample holder within a rotary-shear apparatus to simulate high-velocity slip in water-saturated serpentinite gouges. The principal objective of our study was to investigate the influence of fluid drainage on the frictional behavior of serpentinite gouges and the associated phase transformations within the slip zone. Our findings provide new insights into coseismic slip processes in serpentinite-bearing faults, and also have implications for interpreting coseismic slip indicators in natural

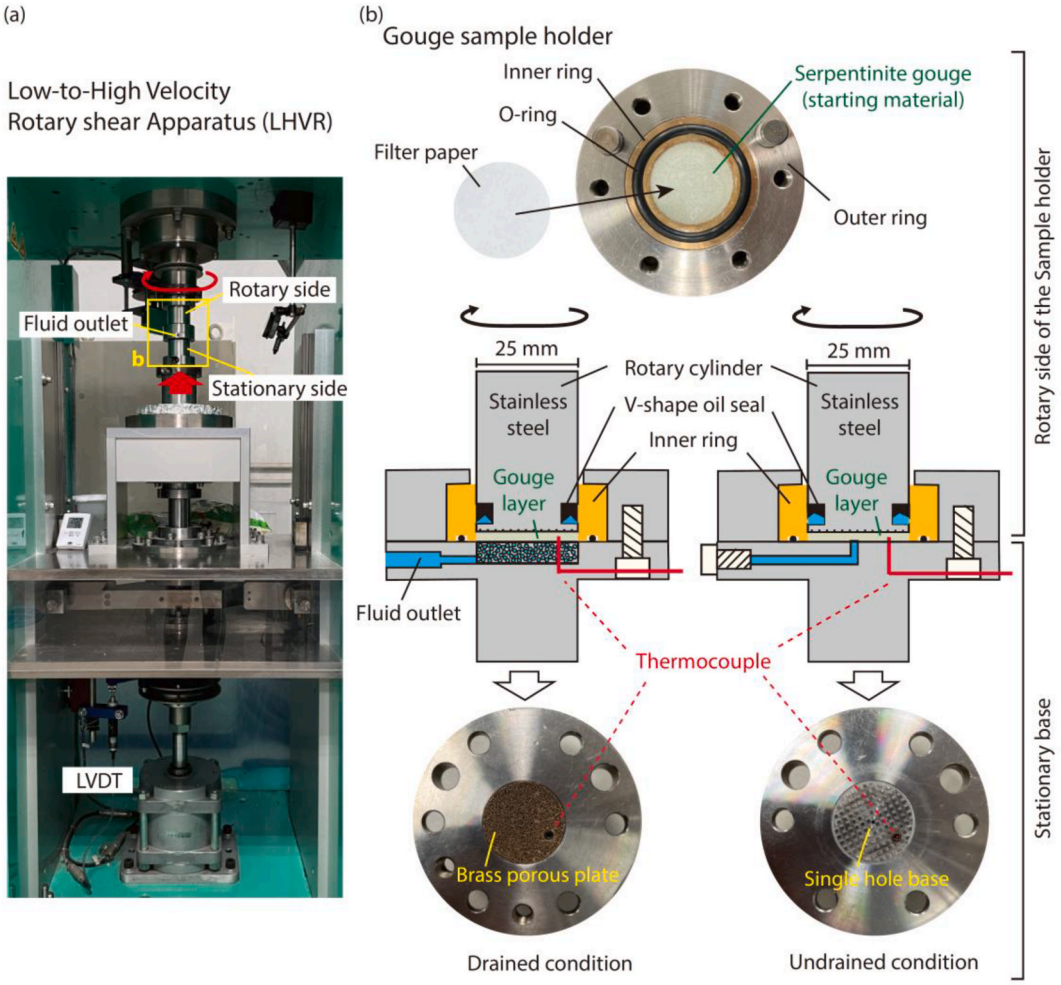

Fig. 1. The purpose-built sample holder and the low-to-high velocity rotary shear apparatus (LHVR) at NCU, Taiwan. (a) Photograph of LHVR equipped with the assembled gouge holder. (b) Photograph and scale diagram of disassembled gouge holder for fluid-drained/undrained conditions. LVDT stands for linear variable differential transformer.

serpentinite-bearing structures.

2. Experimental procedures

2.1. High-velocity experiments and gouge sample holder

The Yuli Belt in Taiwan has been proposed as a metamorphosed subduction mélange containing antigorite-dominated serpentinite (Yen, 1963; Chen et al., 2017). Therefore, we collected samples of natural serpentinite rock from the Yuli Belt in Taiwan (Yen, 1963) and used a low-to-high velocity rotary shear apparatus (LHVR) at the Department of Earth Sciences at the National Central University in Taiwan (Fig. 1a; Kuo et al., 2021). The serpentinite is composed of >95 % antigorite, as well as minor amounts of chrysotile and talc (also used in Hirose and Bystricky, 2007). Given that fracturing and comminution occur in the PSZ during rupture propagation and the initial stages of coseismic slip (e.g., Di Toro et al., 2009), most of the coseismic slip is expected to occur within comminuted and incohesive fault gouge materials. We pulverized the serpentinite samples and sieved them to a grain size of <125 μm for the high-velocity friction experiments. In addition, because we used a rotary configuration, the equivalent slip rate (V) is defined as the slip rate at two-thirds of the gouge radius, as outlines by Hirose and Shimamoto (2005):

$$V = \frac{4\pi R(r_{ext}{}^2 + r_{ext}r_{int} + r_{int}{}^2)}{3(r_{ext} + r_{int})}$$

where R is the revolution rate of the motor (rpm) and r_{ext} and r_{int} are, respectively, the external (12.5 mm) and internal (0 mm) radius of the gouge layer. As we did not measure the pore fluid pressure during the experiments, we calculated the "apparent" friction coefficient by dividing the shear stress (τ, converted from the measured torque) by the applied normal stress (σ_n).

We used a sample holder that enabled us to shear the gouge samples in water-saturated conditions at high slip rates and normal stresses (Kuo et al., 2021). The sample holder has a cross-hatched stainless-steel rotary cylinder, a phosphor brass ring, an outer ring, and a stainless-steel stationary base plate (Fig. 1b). For each experiment, 2 g of serpentinite powder was mixed with boiled tap water and sandwiched between the rotary cylinder and the stationary base. In fluid-drained and undrained experiments, we used either a porous copper stationary base plate (Kuo et al., 2022a; bottom-left panel in Fig. 1b) or a single-hole stationary base plate (Kuo et al., 2021; bottom-right panel in Fig. 1b), respectively. To prevent gouge extrusion from the fluid outlet during the experiments, filter paper was placed between the gouge and the stationary base plate. Before shearing, we manually compacted the gouge layer until we observed fluid draining from the fluid outlet. This ensured that the experiments were conducted under water-saturated conditions.

After loading the sample holder into the LHVR, the gouge was compacted at a normal stress of 1 MPa and pre-sheared at $V = 1$ mm/s for 100 s to minimize the pressurization effect caused by compaction (Faulkner et al., 2018). During this stage, the pore fluid could drain freely through the fluid outlet. The load was then increased to the desired normal stress of 10 MPa and the gouge thickness was allowed to stabilize (>1 h). No gouge extrusion was observed during this stage. The initial gouge layer thickness for all experiments was 1.7 ± 0.2 mm before shearing. We recorded the mechanical data at a frequency of 1 kHz. In this paper, we present the apparent friction coefficient without subtracting the contribution of intrinsic friction derived from the sample holder. This is because the intrinsic friction at > 2 MPa normal stress is negligible and does not influence the interpretation of the friction data (Kuo et al., 2022a).

The evolution of frictional heat within the gouge layer is critical for the initiation of thermally driven processes (e.g., Nguyen et al., 2024). Two of the experiments (one under drained conditions and one under undrained conditions) were conducted using a thermocouple to investigate temperature evolution with displacement (Table 1). In these experiments, a sheathed K-type thermocouple (Ni-Cr wires) was embedded in the stationary base plate at a radial distance of ~8.3 mm from the center of the gouge layer (~two-thirds of the gouge layer radius; Fig. 1b). The tip of the thermocouple was located at ~0.5 mm from the margin of the gouge layer. Microstructural observations described below indicate that the thermocouple tip was ~1 mm from the PSZ that formed during the experiments.

2.2. Analytical methods

Following the experiments, the gouge layers that had been sheared in fluid-undrained conditions were found to be poorly cohesive. In contrast, those that had been sheared in fluid-drained conditions were relatively dry and cohesive. The experimental products were left to dry at room temperature and humidity, and then impregnated with epoxy resin. We prepared petrographic thin sections for observations in a field emission scanning electron microscope equipped with an energy dispersive spectrometer (FESEM/EDX) at the National Central University in Taiwan. Thin sections were cut perpendicular to the gouge layer and sub-parallel to the slip direction. We found that samples sheared under identical experimental conditions exhibited similar microstructural characteristics. For this reason, we focus here on presenting SEM observations of a thin section of sample LHVR 1620 (undrained) and LHVR1606 (drained).

In situ synchrotron XRD analysis of petrographic thin sections results in a bump in the XRD spectra due to penetration of the glass thin sections (e.g., Fig. 4a in Kuo et al., 2014). Here, we analyze rock slices to eliminate the contribution of the bump from the petrographic thin section. Slices cut perpendicular to the margins of the gouge layers were prepared for in-situ synchrotron X-ray diffraction (XRD; beamline BL01C2) at the National Synchrotron Radiation Research Center (NSRRC) in Taiwan. The slices were analyzed with X-rays at a wavelength of 0.774910 Å, an electron beam energy of 1.5 GeV, and a beam size of 100 μm diameter (e.g., Hung et al., 2019; Wu et al., 2020). In addition, we used the high-resolution dual-beam FIB system (FEI Versa 3D model at the National Central University, Taiwan) with a high-energy gallium ion beam to prepare thin foils ~3 × 6 μm in size from inside the PSZ of thin section LHVR1445 (drained). The thin foils were analyzed with a JEM-2000FXII transmission electron microscope at the National Central University, Taiwan.

3. Results

3.1. Mechanical data

All of the experiments were conducted at a slip rate (V) of 1 m/s and a normal stress of 10 MPa (Table 1). Representative mechanical data under fluid-drained and undrained conditions are plotted in Fig. 2, including the apparent friction coefficient (μ), slip rate (V), axial displacement, and temperature. We determine the values of peak friction (μ_p) and steady state friction (μ_{ss}) by averaging μ within a slip interval (see rectangles in Fig. 2).

In the fluid-undrained experiment, μ_p reached a value of ~0.33 within the first ~0.6 m of displacement and decreased to ~0.09 after ~3.0 m, where it remained until the end of the experiment (Fig. 2a). The gouge layer gradually compacted by ~0.26 mm up to a displacement of ~6 m, and then slightly dilated at the end of the experiment. The temperature rapidly reached ~150 °C within ~1.4 m displacement, slightly decreased to ~128 °C after ~2 m displacement, and then gradually increased to reach a maximum value of ~180 °C at the end of the experiment.

In the fluid-drained experiment, a relatively constant μ_p of ~0.42 was observed between ~0.5 and 1.5 m. This was followed by a drop to μ_{ss} of ~0.19 after ~2.4–3.0 m, and then an increase to ~0.29 by the end of the experiment (Fig. 2b). The gouge layer compacted by ~0.33 mm in

Table 1
List of experiments, experimental conditions, and mechanical data.

Experiment	Drainage Condition	Ambient condition	σ_n (MPa)	Average Peak friction μ_p	Average steady state μ_{ss}	Slip velocity V (m/s)	Total slip D (m)	Acceleration/ Deceleration (m/s^2)	Temperature measurement
LHVR1445	Drained	WS	10	0.37	0.29	1.0	6	3.5	N
LHVR1606	Drained	WS	10	0.42	0.28	1.0	4	3.5	Y
LHVR1486	Undrained	WS	10	0.32	0.12	1.0	5.25	3.5	N
LHVR1620	Undrained	WS	10	0.33	0.09	1.0	6.97	3.5	Y

WS, water-saturated.

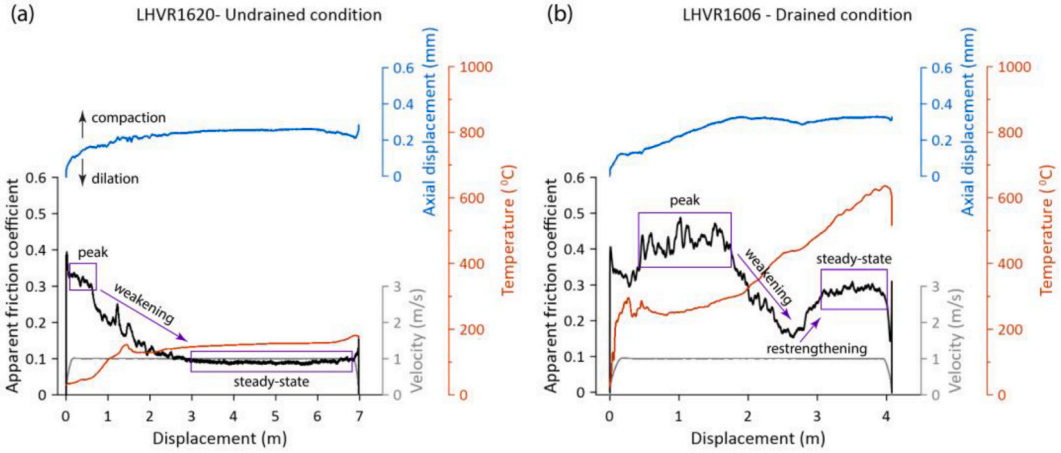

Fig. 2. Experiments conducted with LHVR on wet serpentinite powders at a velocity of 1 m/s and normal stress of 10 MPa. The apparent friction coefficient (shear stress/normal stress) versus displacement is shown for experiments performed under (a) fluid undrained and (b) drained conditions. Frictional evolution, axial displacement, and velocity with displacement are shown for two experiments (in black, blue, and grey curves, respectively). The measured temperature evolution near the PSZ is shown by red lines. (For interpretation of the references to colour in this figure legend, the reader is referred to the Web version of this article.)

the first ~2.0 m of slip but then dilated by ~0.03 mm between ~2.0 and 2.5 m, a change that coincides with the observed friction drop. During the frictional restrengthening stage, the gouge compacted again by ~0.02 mm. The temperature increased to ~300 °C at the onset of the experiment and remained steady during the constant μ_p stage. Following this, the temperature gradually increased to ~450 °C during frictional weakening and reached its maximum value of ~635 °C by the end of the experiment.

3.2. Microanalysis

3.2.1. Synchrotron X-ray diffraction

Following the fluid-drained experiments, the surface of the gouge layer adjacent to the rotary side of the sample holder has a black outer edge (Fig. 3a). In contrast, after the fluid-undrained experiments, the surface of the gouge layer is pale green, similar to the starting material (Fig. 3a). Under cross-polarized light, the compacted and pre-sheared gouges contain randomly oriented, sub-rounded clasts of serpentine (yellowish area; Fig. 3b). There is a slight reduction in grain size close to the rotary side. The dark area in Fig. 3b is an artefact resulting from the thickness of the section. The sheared gouges become dark or opaque close to the rotary side, while close to the stationary side, they are yellow and similar to the starting material (Fig. 3c and d). These observations suggest that strain localization occurs closer to the rotary side of the sample holder (Fig. 3b–d), which is consistent with previous studies by Kuo et al. (2021, 2022a) and Nguyen et al. (2024). We focus on characterizing the deformed gouge layers close to the rotary side, which contain the PSZ.

Because the equivalent velocity is estimated at two-thirds of the gouge radius, in-situ synchrotron X-ray diffraction was performed in approximately this position using thin slices of the deformed gouge layers. We collected observations along profiles from the rotary side to the stationary side. We also analyzed the starting materials. Fig. 3 shows representative XRD results from undrained (Fig. 3e) and drained (Fig. 3f) experiments from i) deformed gouges within the PSZ (red curves), ii) weakly deformed gouges from the stationary side of the gouge layers (blue curves), and iii) the starting material (black curves). As synchrotron XRD on powdered materials yields higher intensities than thin slices of gouge, we plot the XRD results using different intensity scales for easy comparison.

The starting materials consist mainly of antigorite, together with minor chrysotile, lizardite, and talc (Fig. 3e and f). In undrained conditions (LHVR1486) our XRD results from both the PSZ and the stationary side are dominated by the serpentine group minerals and talc, suggesting no significant change in composition compared to the starting materials. Instead, in drained conditions (LHVR1445) we detected strong peaks for olivine and enstatite within the experimental PSZ. Powders from the stationary side contain only the serpentine group minerals and talc, indicating that olivine and enstatite are localized within the PSZ.

3.2.2. Field emission scanning electron microscope

After compaction and pre-shearing, the starting materials contain distributed angular serpentine lamellae <125 μm in size within a fine-grained matrix close to the rotary side (Fig. 4a). In general, the matrix is characterized by platy or sub-rounded grains ~1–2 μm in size (Fig. 4b).

After shearing in undrained conditions (LHVR 1486), the gouge close to the rotary side contains angular serpentine lamellae distributed within a fine-grain matrix, similar to the starting material but with fewer lamellae. In addition, Y shears (i.e., subparallel to the boundaries of the PSZ) are observed (Fig. 4c). Along the Y shears, the platy serpentine grains are slightly reduced in size (<~1 μm) and define a weak foliation (Fig. 4d).

After shearing in drained conditions, a clear PSZ (LHVR 1445) with a relatively constant thickness of ~400–500 μm is formed. A gradual

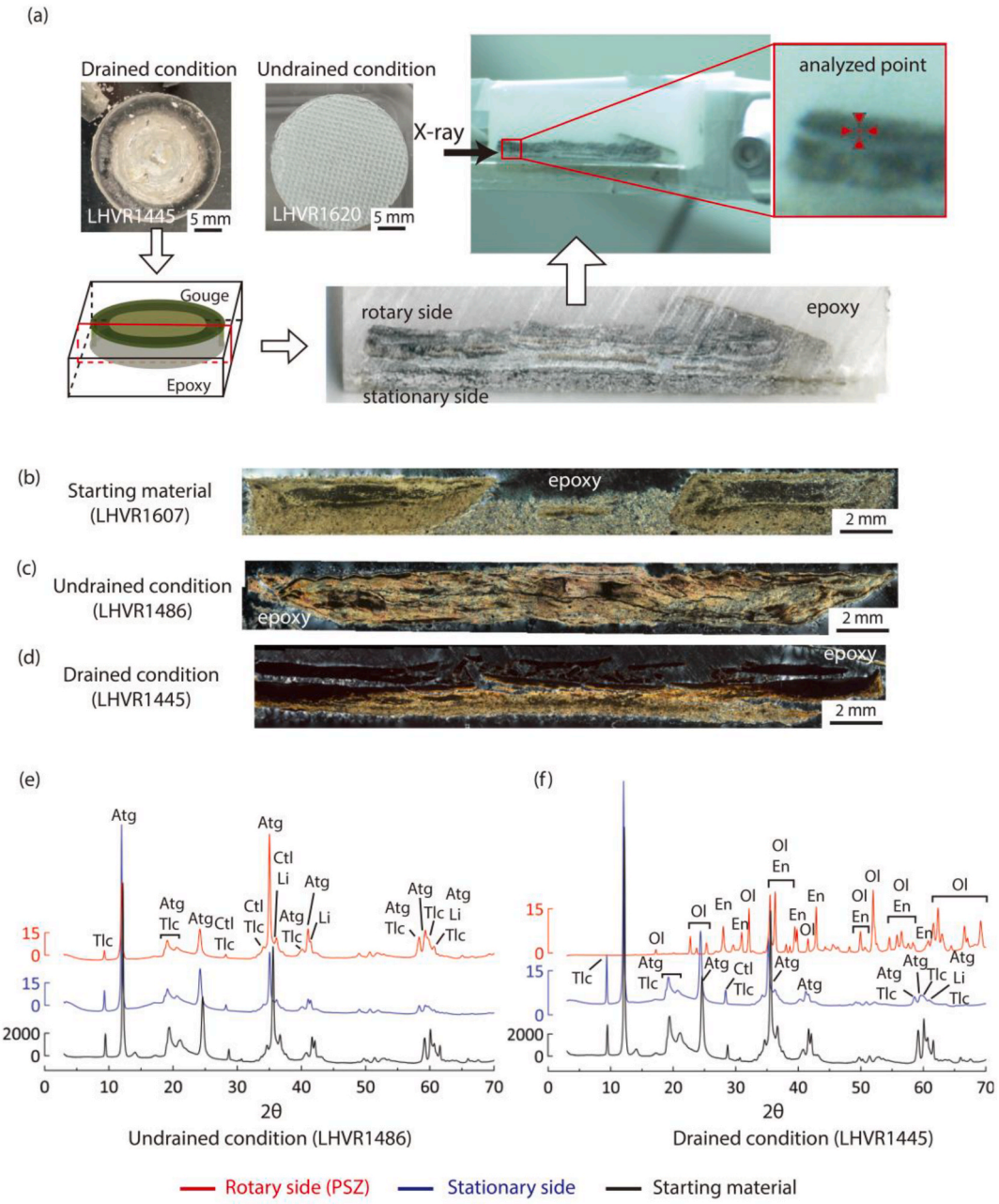

Fig. 3. In situ synchrotron X-ray diffraction patterns from fluid-drained and undrained conditions. (a) The spectra from the PSZ (close to the rotary side) and surrounding materials (close to the stationary side) are obtained from precise locations (in situ) on the thin rock slices (~1.5 mm) without glass slides. The minimum beam size of 150 μm is typically smaller than the PSZ. (b–d) Cross-polarized light observations of experimental products formed by compaction (b) or shearing under undrained (c) and drained (d) conditions. The serpentinite gouge is composed of a localized zone of size-reduced particles and a random distribution of clasts in an optically isotropic, yellowish matrix. (e, f) The minerals within the PSZ formed under undrained and drained conditions can be measured in situ, resulting in a uniform crystallographic orientation instead of random. Mineral abbreviation is adopted from Whitney and Evans (2010), Tlc = talc; Atg = antigorite; Ctl = chrysotile; Li = lizardite; Ol = olivine; En = enstatite.

transition between three distinct microstructural domains is recognized (Fig. 4e). Domain 1 on the rotary side of the PSZ consists of comminuted serpentine, relicts of serpentine lamellae, and a few fragments with nanometric vesicles. The boundary between domains 1 and 2 is subtle (Fig. 4f). Domain 2 contains ultrafine-grained material that shows cracks and nanometric vesicles (Fig. 4g and h) and is cut by Y shears. As described below, this domain contains serpentine decomposition products (Fig. 3f). Domain 3 consists of weakly deformed serpentine lamellae (domain 3 shown in Fig. 4f is the upper boundary of the relatively weakly deformed region).

3.2.3. *Focused ion beam transmission electron microscope*

For a more detailed characterization of the PSZ, thin foils for TEM analysis were collected directly from the PSZ (domain 2) that formed in drained conditions (LHVR1445). Results from the bright field image and the selected area diffraction pattern (SAED) show that the PSZ is mainly composed of an amorphous matrix material containing subhedral to anhedral grains of olivine and enstatite tens and hundreds of nanometers in size (Fig. 5a). Olivine is slightly larger and rather homogeneous compared to enstatite, which is characterized by a well-defined internal lamellar structure. Nanocrystalline olivine and enstatite from a slip zone within the Livingstone Fault are shown for comparison and described in

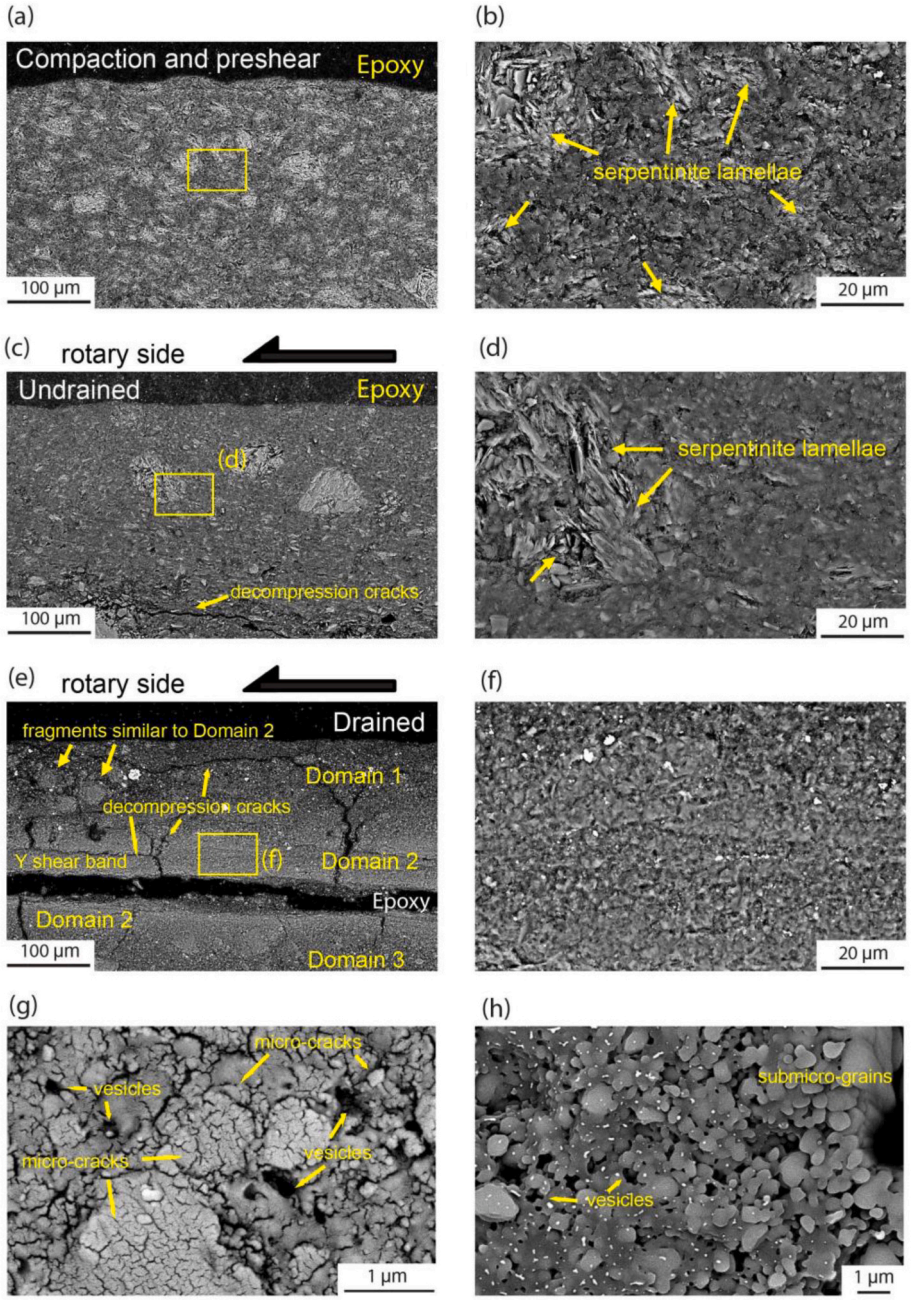

Fig. 4. SEM images of water-saturated serpentinite gouge layers. (a, c, e) Microstructures of the gouge layer close to the rotary side (i.e. PSZ) from both compacted and sheared serpentinite gouges under fluid-drained and undrained conditions. Starting materials were compacted at 10 MPa. The selected areas are enlarged in (b, d) showing grain size reduction under compaction/preshear and fluid-undrained conditions, respectively. (f) The selected areas exhibit reduced porosity and diffuse grain boundaries. (g, h) The selected area of the PSZ under drained conditions (LHVR 1445), showing micro-cracks, vesicles, and submicron-sized grains.

more detail below (Fig. 5b and c).

4. Discussion

4.1. Temperature evolution during the experiments

To test whether a thermal pulse during the experiments could cause dehydroxylation and amorphization, 1D finite-element modeling was used to quantify the effects of frictional heating. The numerical modeling was performed using the COMSOL Multiphysics software package. Model boundaries were constructed several centimeters away from the region of interest so that they do not induce boundary effects. The PSZ is represented as a volumetric frictional heat source within the slip zone and lies along an edge between the serpentinite layer and the stainless-steel rotary cylinder. The interval between B2 and B3 in Fig. 7 represents the gouge layer. The detailed geometry of the gouge layer, including the approximate location of the thermocouple and the thickness of the PSZ, are plotted in Fig. 7b. The initial temperature and pore fluid pressure are set as 20 °C and 1 atm, respectively (Table 2).

Our numerical model is based on the mathematical framework of thermal pressurization and dehydration developed by Rice (2006) and Brantut et al. (2010a,b). When frictional heating occurs within the gouge, several coupled physical and chemical processes govern the evolution of heat generation and transfer. For example, frictional heating leads to pore fluid expansion and an increase in pore fluid pressure, which results in thermal pressurization and prevents a temperature rise.

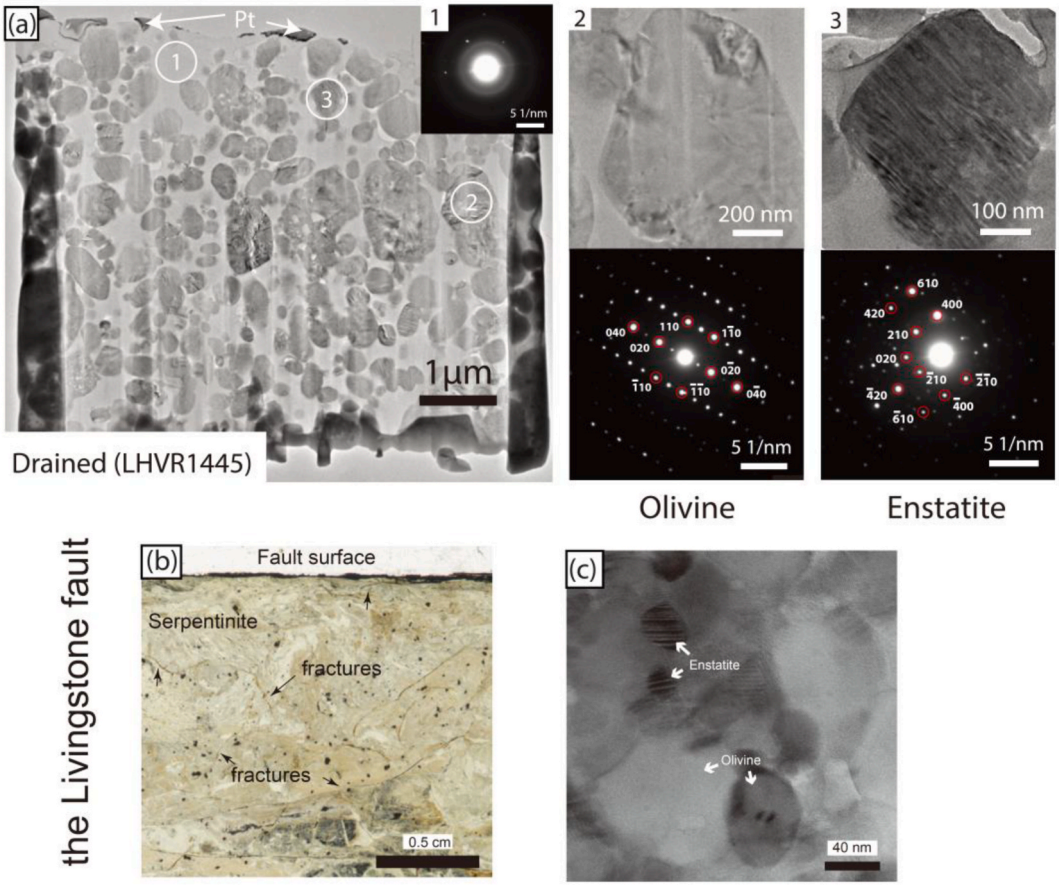

Fig. 5. FIB-TEM images of the PSZ from both fluid-drained conditions (experiment LHVR 1445) and a natural serpentinite-bearing shear zone. (a) Serpentine dehydroxylation and amorphization in the experimental PSZ (field-emission scanning electron microscopy [SEM] images). Circular insets show (1) the presence of amorphous material with a diffuse halo and rings caused by amorphous materials in the matrix of the PSZ (selected area electron diffraction [SAED] pattern), (2) a bright field image of well-crystallized olivine grains (TEM image and SAED pattern), and (3) a bright field image of well-crystallized enstatite (TEM image and SAED pattern). (b) Petrographic thin section of a polished fault surface from the Livingstone Fault in New Zealand. The fault surface contains a thin magnetite layer adjacent to serpentinite (Tarling et al., 2018). (c) Crystalline nanograins of olivine and enstatite within the Livingstone Fault (Tarling et al., 2018).

On the other hand, serpentinite dehydroxylation leads to reaction-enhanced porosity formation. This creates a porosity front that advances as serpentinite dehydroxylation progresses. The increase in porosity leads to an increase in local fluid storage capacity, reducing the effectiveness of thermal pressurization.

The model includes one-dimensional heat diffusion during frictional heating, the dehydroxylation enthalpy of serpentinite, thermal pressurization of pore fluids in a poroelastic medium, and fluid production during serpentinite dehydroxylation and the resulting thermochemical pressurization. A full treatment including the governing equations can be found in Lachenbruch (1980), Rempel and Rice (2006, 2006), and Brantut et al. (2010). Model parameters are presented in Table 2. We model the dehydration and dehydroxylation of serpentinite by considering it as a phase change using the COMSOL Phase Change Material node in the heat transfer module, and approximated the dehydroxylation reaction as serpentinite to forsterite (Tarling et al., 2018). The pore fluid pressure is calculated using the fluid mass conservation equation, which accounts for the pressurization of fluid by heating, fluid flow away from the fault, poroelasticity, and fluids and porosity produced by the dehydration reactions (Tarling et al., 2018). As a first-order numerical approximation, this model does not include fluid flow, possible deformation effects (non-poroelastic effects), shear-induced compaction or dilatancy, reaction-induced porosity change, and increased permeability due to reaction-induced porosity. As a result, the model does not fully capture the thermal evolution of the system, but instead provides an estimate of the peak temperature reached, based on the bulk mechanical work input and the thermal properties of the system. The modelling results show a rapid temperature increase close to the boundary between the rotary side and the gouge layer. However, the phase change implementation for the vaporization of pore fluid, without explicit two-phase fluid flow, does not capture the temperature buffering effect of saturated steam observed in both the drained and undrained experiments, or the rapid transport of heat to the thermocouple due to the advective transport of vaporized pore water.

4.1.1. *Fluid-undrained conditions*

In fluid-undrained conditions, the modeled temperature at the thermocouple reaches ~160 °C after ~1.4 m of slip, similar to the measured temperature (see Fig. 6c). Subsequently, the modeled temperature gradually increases to reach a maximum of ~200 °C by the end of the experiment, which is slightly higher than the measured value. This suggests that the modeled temperature during steady state is overestimated by ~20 °C. The modeled temperature in the PSZ increases rapidly to ~370 °C after <1 m of slip. It then gradually increases to ~400 °C before slightly decreasing to reach a steady state of ~380 °C by the end of the experiment (Fig. 6c). Because the pore fluids have higher thermal expansion and higher thermal conductivity than the powders, frictional heating causes an increase in pore pressure and a corresponding decrease in shear strength, described as thermal pressurization (Rice, 2006; Wibberley and Shimamoto, 2005) or water vaporization (Chen et al., 2017a, 2017b).

Based on the pressure-temperature conditions of the water phase

Table 2
Values for parameters used in the numerical model. Parameters without specific values are temperature/pressure dependent. The references provide the temperature/pressure relationships used.

Parameter	Value
Porosity of gouge	0.3
Density of serpentinite	2600 kg m^{-3}
Permeability of serpentinite gouge	10^{-17} m^2 (Brantut et al., 2010a,b)
Heat capacity of serpentinite	J kg^{-1} K^{-1} (Osako et al., 2010)
Thermal conductivity of serpentinite	W m^{-1} K^{-1} (Seipold and Schilling, 2003)
Density of forsterite	3200 kg m^{-3}
Heat capacity of forsterite	J kg^{-1} K^{-1} (Xu et al., 2004; Cynn et al., 1996)
Thermal conductivity of forsterite	W m^{-1} K^{-1} (Xu et al., 2004; Cynn et al., 1996)
Density of water	1000 kg m^{-3} (Wagner and Pruβ, 2002)
Viscosity of water	Pa s (Huber et al., 2009)
Thermal expansion of water	K^{-1} (Wagner and Pruβ, 2002)
Compressibility of water	Pa^{-1} (Wagner and Pruβ, 2002)
Thermal conductivity of porous ceramic	10 W m^{-1} K^{-1} (Kuo et al., 2022a).
Density of porous ceramic	5000 kg m^{-3} (Kuo et al., 2022a)
Porosity of porous ceramic	0.4 (Kuo et al., 2022a)
Specific heat of porous ceramic	700 J kg^{-1} K^{-1} (Kuo et al., 2022a)
Permeability of porous ceramic	10^{-13} m^2 (Kuo et al., 2022a)
Thermal conductivity of stainless steel (304 SS)	16 W m^{-1} K^{-1} (Kuo et al., 2021)
Density of stainless steel (304 SS)	8000 kg m^{-3} (Kuo et al., 2021)
Porosity of stainless steel (304 SS)	0.0005 (Kuo et al., 2021)
Specific heat of stainless steel (304 SS)	500 J kg^{-1} K^{-1} (Kuo et al., 2021)
Saturated hydraulic conductivity of stainless steel (304 SS)	1.1×10^{-23} m s^{-1} (Kuo et al., 2021)
Initial temperature	20 °C
Enthalpy heat of serpentine dehydration	521 kJ mol^{-1} (Llana-Fúnez et al., 2007)

diagram (Chen et al., 2017a, 2017b; Weatherley and Henley, 2013), the modeled PSZ temperature (~370 °C as the upper bound) should cause vaporization of water within the PSZ. As slip evolves, the temperatures increases to >350 °C (Fig. 6c), allowing water to transition from fluid to vapor, leading to thermal expansion, vaporization and thermal pressurization. Both vaporization and thermal pressurization can result in high pore fluid pressures and an associated decrease in the effective normal stress (e.g., Aretusini et al., 2021). These are likely to be the main dynamic weakening mechanisms in undrained conditions, consistent with data from other compositions of gouge (Chen et al., 2017a; Nguyen et al., 2024). However, water vaporization is predicted to result in dramatic dilation of the gouge layer, as the density of water vapor can be three orders of magnitude lower than that of liquid water under the same conditions (Chen et al., 2017a). Here, the continuous compaction of the gouge layer up to ~2 m of slip (Fig. 2a) suggests that water vaporization was relatively minor or negligible under fluid-undrained conditions. Furthermore, it has been proposed that the pore pressure increases much faster than the temperature, and that the pore fluid cannot vaporize before entering the supercritical phase (Kuo et al., 2021), suggesting that vaporization can be inhibited by thermal pressurization in low permeability gouges (Chen et al., 2017b).

Because the fluid is confined to the sample holder in undrained conditions, thermal pressurization presumably continues to inhibit the temperature rise and follows a constant temperature plateau, as observed in both the modeled and measured temperatures (Fig. 6c). When compared to gouge samples sheared under identical conditions (fluid undrained, slip rate of 1 m/s, and normal stress of 10 MPa) with the same gouge sample holder, Kuo et al. (2021) showed a similar temperature plateau (with a pore pressure of ~4 MPa) during the experiment (iFg. 12c in Kuo et al., 2021) and suggested thermal pressurization as the weakening mechanism. Therefore, although our modeling does not constrain the pore fluid pressure, thermal pressurization is likely to be the weakening mechanism during the experiments. Our results are also consistent with previous studies suggesting thermal pressurization as a mechanism to control the evolution of shear strength during seismic slip in gouge experiments (Ferri et al., 2011; Aretusini et al., 2021; Nguyen et al., 2024).

In both natural and experimental examples, thermal pressurization has been interpreted to result in clay particle rotation and movement in suspension (Boullier et al., 2009; Kuo et al., 2021, 2022b). The lack of strain localization and the random fabric of serpentine lamellae observed after the experiments (Fig. 4c) is consistent with the interpretation that the gouge layers were fluidized due to thermal pressurization (Boulton et al., 2017; Kitajima et al., 2010; Ujiie et al., 2011), and is also compatible with previous studies showing that thermal pressurization maintains sliding at relatively low temperatures (e.g., Acosta et al., 2018).

4.1.2. *Fluid-drained conditions*

Under fluid-drained conditions, the modeled temperature at the thermocouple gradually increases to reach a maximum value of ~600 °C by the end of the experiment, which is slightly lower than the measured

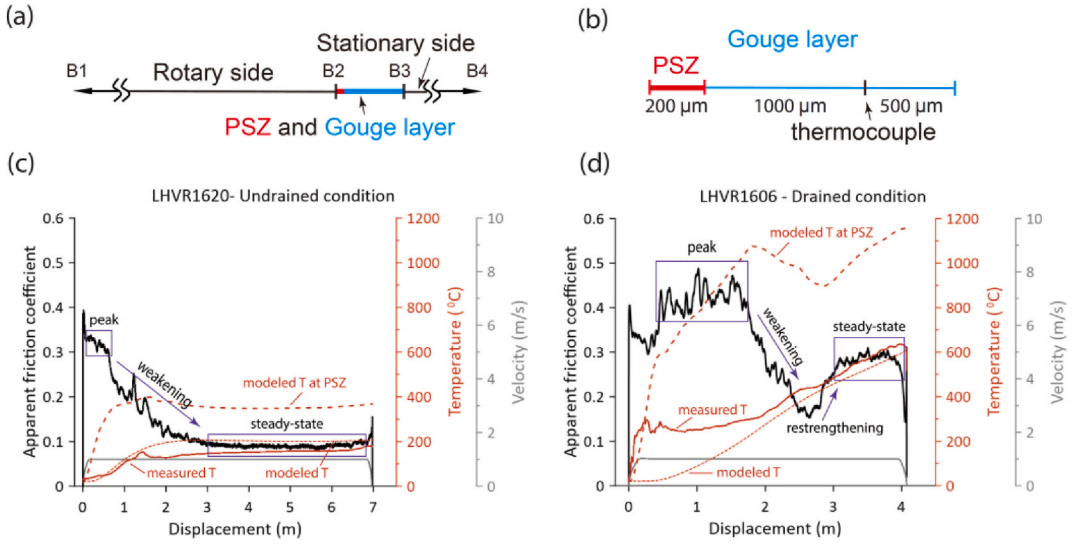

Fig. 6. 1D model of frictional heating during experiments under drained and undrained conditions. (a, b) Schematic of the 1D model. (c, d) Modeled and measured temperature evolution at the thermocouple and within the PSZ shown together with the mechanical data.

value (Fig. 6d). Due to the lack of two-phase fluid flow in our model, the modeled temperature may be underestimated at the thermocouple position. On the other hand, the modeled temperature in the PSZ rapidly increases to ~1100 °C after ~2.0 m of slip, gradually decreasing to ~900 °C at ~3.0 m of slip and then increasing to ~1150 °C by the end of the experiment (Fig. 6d). Both the peak and steady-state friction values are higher than under fluid-undrained conditions (Fig. 2; Table 1). This suggests that thermal pressurization and water vaporization are less efficient processes under fluid-drained conditions.

In drained conditions, a gradual reduction in pore fluid pressure likely suppresses thermal pressurization (Nguyen et al., 2024). This behavior is supported by experimental observations of alternating gouge dilation and compaction (Fig. 2b). During the frictional weakening phase, the temperature increases to approximately 311 °C, which is the expected vaporization temperature at 10 MPa normal stress. This corresponds to the maximum pore pressure sustained under the nominal normal stress of 10 MPa. At this stage, dilation transitions to compaction, implying enhanced fluid mobility, possibly due to increased pore interconnectivity. Once compaction ceases, restrengthening is observed, coincident with a further temperature increase. This restrengthening likely reflects the development of a load-bearing granular framework that is no longer lubricated by interstitial fluids. In addition, as shearing progresses, the serpentinite powders become intensely comminuted, resulting in an increase in the grain contact area and an associated increase in shear heating between grains. At this stage, increased frictional heating between grains at high slip rates (e.g., Kuo et al., 2022a) can achieve the temperatures necessary to trigger dehydroxylation and amorphization of serpentinite to produce olivine and enstatite (Figs. 3 and 5).

At temperatures >650 °C, the dehydroxylation and amorphization of serpentine releases water (Brindley and Hayami, 1965; Melekhova et al., 2006):

$$\text{Serpentine} \rightarrow \text{Olivine} + \text{Enstatite} + 2H_2O \quad (1)$$

The dehydroxylation reaction within the PSZ and the release of water both absorb frictional heat, which is consistent with the modeled temperature decrease at this stage. This suggests that dehydroxylation and amorphization occurred during fluid-drained conditions (Fig. 2b, 3 and 4g, h). Subsequently, the dehydroxylation of serpentine was complete and frictional heat gradually accumulated, resulting in an increase in temperature towards the end of the experiment.

Domain 2 (Fig. 4e) within the PSZ exhibits reduced porosity and diffuse grain boundaries, typical annealing textures (Viti and Hirose, 2010). TEM observations from domain 2 show highly crystalline olivine and enstatite (Fig. 5), which may have crystallized either during or following slip (i.e., during frictional heating or post-slip cooling). Static heating experiments on serpentinite-group minerals (e.g., Viti, 2010; heating step of 10 °C/min and temperature range of 0–1000 °C) show that antigorite dehydrates over a wide temperature range from 650 °C to 750 °C. Forsterite crystallization begins close to 750 °C before antigorite dehydration is complete. Enstatite crystallizes within a narrower temperature window between 820 and 830 °C and forms from completely dehydrated material. The slightly larger grain size of olivine within domain 2 is in agreement with the above crystallization sequence. The presence of enstatite also suggests that the temperature within the PSZ (i.e., domain 2) was at least 820 °C, consistent with the model proposed in the previous paragraph.

It should be noted that the gouges within the PSZ were also subject to grain interactions and rubbing during frictional sliding. Wear induces tribochemical reactions that result in increased surface area and reduced grain size. This process can lead to the formation of new compounds, as well as trigger dehydration and dehydroxylation reactions in the case of clays (Kuo et al., 2011; Aretusini et al., 2019). This suggests that tribochemical reactions may occur at lower activation energies (and thus their kinetics is more efficient at a given temperature) than thermochemical reactions (Steinike and Tkácová, 2000). Thus, considering the effects of tribochemical reactions, the suggested temperature achieved within the PSZ might be overestimated.

4.2. Comparison to previous high-velocity experiments on serpentinite

Due to a lack of high-velocity experiments conducted on fluid-bearing serpentinites, we compare our mechanical data with previous experiments performed under relatively dry conditions (Table 3). The results of Hirose and Bystricky (2007) showed a reduction in the friction coefficient from ~0.40 to ~0.11. Similarly, Kohli et al. (2011) conducted experiments on cohesive serpentinite at normal stresses of 5 MPa and a slip velocity of 0.30 m/s, observing an initial increase in the friction coefficient to 0.71 followed by a dramatic drop to 0.26. Lin et al. (2013) sheared serpentinite under comparable conditions (normal stresses of 5–8 MPa and velocities of 0.35–1.30 m/s) and documented a decrease in the friction coefficient from ~0.35 to 0.55 to ~0.20–0.30. Proctor et al. (2014) demonstrated that the steady-state friction of serpentinite gouge decreased from ~0.51 to ~0.35 as normal stress increased from 4 to 22 MPa, which was higher than the steady-state values for cohesive serpentinite rocks (~0.09–0.14) at normal stresses ranging from 5 to 97 MPa. In all of these experiments, water released during serpentine dehydroxylation was expelled freely from the PSZ. Therefore, these studies indicate that the extreme dynamic weakening of serpentinites (whether cohesive rock or non-cohesive gouge) under dry conditions is likely due to flash heating at asperity contacts.

Our mechanical data demonstrate dynamic weakening under wet conditions (Fig. 2; Table 3) and broadly agree with findings from previous studies. However, unlike previous work, rapid dynamic weakening due to flash heating was not observed during the initial stages of our experiments (Fig. 2). At the onset of shearing, the serpentinite powders experienced intense comminution, presumably resulting in an increased grain contact area. This may have lead to elevated shear resistance between grains and an increased fluid-grain contact area, inhibiting significant flash heating at grain contacts (Violay et al., 2014). However, flash heating has been proposed as an important mechanism under both room-humidity and wet conditions in serpentinite and other silicate rocks (Hirose and Bystricky, 2007; Tisato et al., 2012; Violay et al., 2014). It is possible that a flash-type heating mechanism may have played a role in the shear heating processes that ultimately triggered thermal pressurization in our study.

While serpentine dehydroxylation occurred in all of our experiments with power densities >0.3 MW/m^2 (i.e. shear stress x velocity), the formation of olivine and enstatite was only observed at displacements exceeding tens of centimeters (Table 3). In contrast, experiments with shorter displacement slip events (ranging from millimeters to centimeters) mainly triggered serpentine dehydroxylation into amorphous materials (Brantut et al., 2016) or talc (Kohli et al., 2011). This is likely due to the limited slip, which was insufficient to trigger conventional mineral crystallization reactions (e.g., formation of olivine and enstatite).

All of our experiments were conducted over large displacements (> several meters) and power densities exceeding 0.9 MW/m^2. However, serpentine dehydroxylation and the formation of olivine and enstatite were observed only under fluid-drained conditions (Fig. 5c and 6). This suggests that under fluid-undrained conditions, thermal pressurization within the PSZ suppresses the temperature increase (Fig. 3a and 7a) necessary to cause serpentine dehydroxylation (Fig. 3e). In contrast, under fluid-drained conditions, the PSZ gradually became dry at high slip velocities. As slip continued, the drying of the PSZ facilitated a temperature increase (Fig. 6b), which subsequently initiated serpentine dehydroxylation (Fig. 3c and 5). Our observations are consistent with previous studies, which indicate that serpentine dehydroxylation is triggered under relatively dry conditions (references in Table 3). Therfore, we demonstrate that fluid-drained conditions are critical for serpentine dehydroxylation and the formation of olivine and enstatite during experimental seismic slip.

Table 3
List of experiments, experimental conditions, mechanical data, and experimental products reported in previous studies.

	Rock type	Sample Condition (experiment no.)	Normal stress (MPa)	Velocity (m/s)	Displacement (m)	μ_p	μ_{ss}	Powder density (MW/m^2) ($\tau \cdot v$)	New mineral (after experiments)
Hirose and Bystricky (2007)	rock	dry (HVR694)	24.5	1.1	~3.6	0.4	0.11	3.23	olivine & enstatite
Kohli et al. (2011)	rock	dry (SV300_6)	5	0.30	0.045	0.71	0.26	0.39	talc
Lin et al. (2013)	rock	dry (MH0012 & THVR0110)	5–8	0.35–1.30	42–52	0.35–0.55	0.2–0.3	0.84–1.30	olivine & enstatite
Proctor et al. (2014)	rock	dry (735)	14.9	0.30	0.46	0.66	0.09	0.40	olivine & enstatite
	gouge	dry (824b)	8.5	2	0.51	1	0.35	5.95	olivine
This study	gouge	Wet undrained (LHVR1486)	10	1	7	0.32	0.12	1.20	none
		Wet undrained (LHVR1620)	10	1	7	0.33	0.09	0.90	none
		Wet drained (LHVR1445)	10	1	6	0.37	0.29	2.90	olivine & enstatite
		Wet drained (LHVR1606)	10	1	4	0.42	0.28	2.80	olivine & enstatite

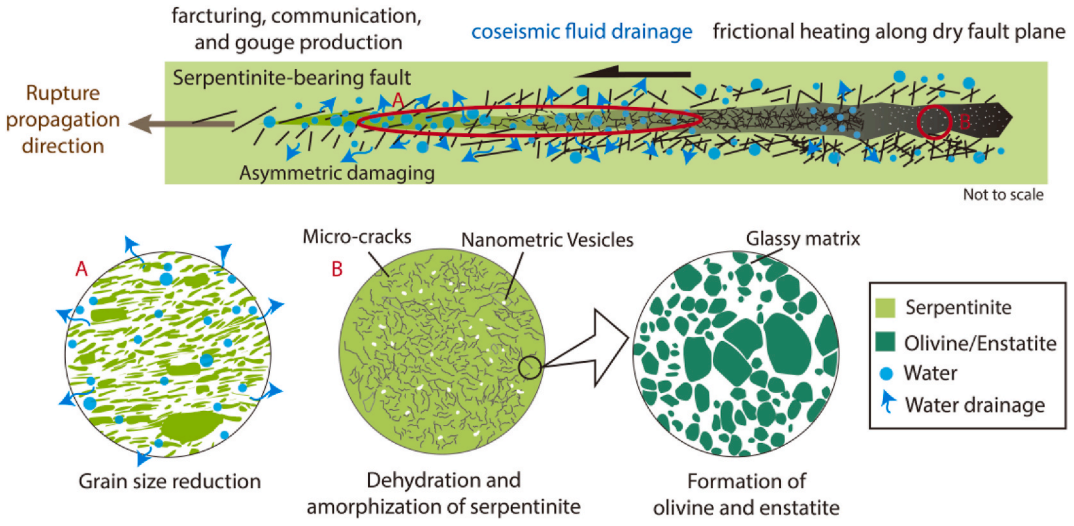

Fig. 7. Schematic model of a Mode II shear rupture propagating through a water-saturated serpentinite-bearing patch (modified from Di Toro et al., 2009). The scenario includes (1) fracturing, comminution, and gouge production near the rupture tip (and asymmetric damage); (2) thermal pressurization of pore water, (3) coseismic fluid drainage through coseismic fractures. Thermal pressurization ceases as frictional slip begins; (4) intense wear continues and serpentinite dehydroxylation occurs, simultaneously releasing water that drains through fractures, (5) bulk dehydroxylation occurs as pore water escapes from the slip zone and a continuous melt layer forms. The red ellipse and circles marked A and B are the observations from the SEM (Fig. 4) and FIB-TEM images (Fig. 5) in this study. (For interpretation of the references to colour in this figure legend, the reader is referred to the Web version of this article.)

4.3. Implications for co-seismic slip

During an earthquake rupture, oscillating stress fields on opposite sides of the rupture plane likely result in the formation of a permeable fracture network (Poliakov et al., 2002; Di Toro et al., 2005). Brantut and Mitchell (2018) suggested that coseismic wall rock damage can transiently increase fault permeability and compressibility by up to 10 times. With continued slip, the generation of tensional fractures allows coseismic fluid drainage and inhibits thermal pressurization along the PSZ, driving frictional heating and associated physicochemical processes (e.g., the melting process in Di Toro et al., 2005). Based on our results and previous studies (Di Toro et al., 2009; Yao et al., 2023), a schematic plot of a mode II shear rupture propagating through a wet serpentinite-bearing fault patch is presented (Fig. 7). This model includes (1) fracturing, comminution, and gouge production near the rupture tip; (2) activation of thermal pressurization of pore water, (3) coseismic fluid drainage through wall rock fractures, lowering the efficiency of thermal pressurization as slip progresses; (4) intense wear and the onset of serpentine dehydroxylation, perhaps initially as a flash process at grain contacts; (5) bulk dehydroxylation (and possible melting) as pore water escapes from the slip zone.

The microstructures and nanocrystalline mineral assemblages recognized in our fluid-drained experiments are similar to those documented in both natural serpentinite-bearing fault zones (Fig. 5b and c; Tarling et al., 2018, 2019b) and previous experiments carried out in relatively dry conditions (references in Table 3). This suggests that dehydroxylation of serpentine can occur as a result of frictional heating in faults and shear zones, but only if the ambient conditions are dry or if co-seismic fluid drainage occurs away from the PSZ. If the slip zone remains water-bearing during coseismic slip, thermal pressurization of pore fluid will inhibit a significant temperature rise and preclude the formation of dehydroxylation products.

5. Conclusions

We sheared wet serpentinite gouges at a slip rate of 1 m/s and normal

stress of 10 MPa under fluid-drained and undrained conditions. In both conditions, thermal pressurization is initiated as a dynamic weakening mechanism. In drained conditions, however, the efficiency of thermal pressurization is progressively reduced with slip, resulting in increased shear heating and an associated increase in temperature within the gouge layer. The microstructures and nanocrystalline mineral assemblages (olivine and enstatite) recognized in our fluid-drained experiments are similar to those documented in natural serpentinite-bearing fault zones and in previous experiments carried out in relatively dry conditions. This suggests that dehydroxylation of serpentinite can occur as a result of frictional heating in faults and shear zones, but only in relatively dry ambient conditions or if coseismic fluid drainage occurs away from the principal slip zone.

CRediT authorship contribution statement

Li-Wei Kuo: Writing – review & editing, Writing – original draft, Visualization, Supervision, Project administration, Methodology, Investigation, Funding acquisition, Conceptualization. **Wei-Hsin Wu:** Methodology, Formal analysis, Data curation. **Matthew S. Tarling:** Writing – review & editing, Software, Formal analysis, Data curation. **Steven A.F. Smith:** Writing – review & editing, Visualization, Validation, Conceptualization. **Thi Trinh Nguyen:** Software, Methodology. **Wen-Jie Wu:** Validation. **Jialiang Si:** Validation, Methodology.

Declaration of competing interest

The authors declare that they have no known competing financial interests or personal relationships that could have appeared to influence the work reported in this paper.

Acknowledgment

We thank the editor Dr. Virginia Toy, Dr. Giacomo Pozzi, and an anonymous reviewer for their detailed and constructive comments. Dr. Hwo-Shuenn Sheu supported the synchrotron XRD analysis at the National Synchrotron Radiation Research Center, Taiwan. Hsiu-Ching Hsiao provided technical support during SEM analysis at the National Central University, Taiwan. Great thanks to Dr. Jia-Jyun Dong for his selfless sharing and endless support of lab resources. This research was supported by the Taiwan ROC (Republic of China) National Science and Technology Council grant NSTC 112-2628-M-008-003 -MY3 and Academia Sinica Scholar Award (grand no. AS-ASSA-113-01) to Li-Wei Kuo. All the experimental raw data are available in Figshare with the identifier at https://figshare.com/articles/dataset/Experimental_mechanical_data_of_serpentinite/30642545?file=59633696.

Data availability

I have shared the link in the manuscript.

References

Andréani, M., Boullier, A.M., Gratier, J.P., 2005. Development of schistosity by dissolution–crystallization in a Californian serpentinite gouge. J. Struct. Geol. 27 (12), 2256–2267. https://doi.org/10.1016/j.jsg.2005.08.004.

Aretusini, S., Plümper, O., Spagnuolo, E., Di Toro, G., 2019. Subseismic to seismic slip in smectite clay nanofoliation. J. Geophys. Res. Solid Earth 124 (7), 6589–6601. https://doi.org/10.1029/2019JB017364.

Aretusini, S., Meneghini, F., Spagnuolo, E., Harbord, C.W., Di Toro, G., 2021. Fluid pressurisation and earthquake propagation in the Hikurangi subduction zone. Nat. Commun. 12 (1), 2481. https://doi.org/10.1038/s41467-021-22805-w.

Bach, W., Paulick, H., Garrido, C.J., Ildefonse, B., Meurer, W.P., Humphris, S.E., 2006. Unraveling the sequence of serpentinization reactions: petrography, mineral chemistry, and petrophysics of serpentinites from MAR 15 N (ODP Leg 209, site 1274). Geophys. Res. Lett. 33 (13). https://doi.org/10.1029/2006GL025681.

Barth, N.C., Boulton, C., Carpenter, B.M., Batt, G.E., Toy, V.G., 2013. Slip localization on the southern Alpine fault, New Zealand. Tectonics 32 (3), 620–640. https://doi.org/10.1002/tect.20041.

Bostock, M.G., Hyndman, R.D., Rondenay, S., Peacock, S.M., 2002. An inverted continental Moho and serpentinization of the forearc mantle. Nature 417, 536–538. https://doi.org/10.1038/417536a.

Boullier, A.M., Yeh, E.C., Boutareaud, S., Song, S.R., Tsai, C.H., 2009. Microscale anatomy of the 1999 chi-chi earthquake fault zone. G-cubed 10 (3). https://doi.org/10.1029/2008GC002252.

Boulton, C., Yao, L., Faulkner, D.R., Townend, J., Toy, V.G., Sutherland, R., Ma, S., Shimamoto, T., 2017. High-velocity frictional properties of Alpine Fault rocks: mechanical data, microstructural analysis, and implications for rupture propagation. J. Struct. Geol. 97, 71–92.

Brantut, N., Mitchell, T.M., 2018. Assessing the efficiency of thermal pressurization using natural pseudotachylyte-bearing rocks. Geophys. Res. Lett. 45 (18), 9533–9541. https://doi.org/10.1029/2018GL078649.

Brantut, N., Schubnel, A., Corvisier, J., Sarout, J., 2010a. Thermochemical pressurization of faults during coseismic slip. J. Geophys. Res. Solid Earth 115 (B5). https://doi.org/10.1029/2009JB006533.

Brantut, N., Schubnel, A., Corvisier, J., Sarout, J., 2010b. Thermochemical pressurization of faults during coseismic slip. J. Geophys. Res. Solid Earth 115, 1–17.

Brantut, N., Passelègue, F.X., Deldicque, D., Rouzaud, J.N., Schubnel, A., 2016. Dynamic weakening and amorphization in serpentinite during laboratory earthquakes. Geology 44 (8), 607–610. https://doi.org/10.1130/G37932.1.

Brindley, G.W., Hayami, R., 1965. Mechanism of formation of forsterite and enstatite from serpentine. Mineral. Mag. J. Mineral Soc. 35 (269), 189–195. https://doi.org/10.1180/minmag.1965.035.269.21.

Cann, J.R., Blackman, D.K., Smith, D.K., McAllister, E., Janssen, B., Mello, S., Avgerinos, E., Pascoe, A.R., Escartin, J., 1997. Corrugated slip surfaces formed at ridge–transform intersections on the Mid-Atlantic Ridge. Nature 385 (6614), 329–332. https://doi.org/10.1038/385329a0.

Chen, W.-S., Chung, S.-L., Chou, H.-Y., Zugeerbai, Z., Shao, W.-Y., Lee, Y.-H., 2017. A reinterpretation of the metamorphic Yuli belt: evidence for a middle-late Miocene accretionary prism in eastern Taiwan. Tectonics 36 (2), 188–206. https://doi.org/10.1002/2016TC004383.

Chen, J., Niemeijer, A., Yao, L., Ma, S., 2017a. Water vaporization promotes coseismic fluid pressurization and buffers temperature rise. Geophys. Res. Lett. 44 (5), 2177–2185. https://doi.org/10.1002/2016GL071932.

Chen, J., Niemeijer, A.R., Fokker, P.A., 2017b. Vaporization of fault water during seismic slip. J. Geophys. Res. Solid Earth 122 (6), 4237–4276. https://doi.org/10.1002/2016JB013824.

Collettini, C., Niemeijer, A., Viti, C., Smith, S.A., Marone, C., 2011. Fault structure, frictional properties and mixed-mode fault slip behavior. Earth Planet Sci. Lett. 311 (3–4), 316–327. https://doi.org/10.1016/j.epsl.2011.09.020.

Cowan, D.S., 1990. Kinematic analysis of shear zones in sandstone and mudstone of the Shimanto belt, Shikoku, SW Japan. J. Struct. Geol. 12 (4), 431–441. https://doi.org/10.1016/0191-8141(90)90032-T.

Cynn, H., Carnes, J.D., Anderson, O.L., 1996. Thermal properties of forsterite, including CV, calculated from αKT through the entropy. J. Phys. Chem. Solid. 57, 1593–1599.

Di Toro, G., Nielsen, S., Pennacchioni, G., 2005. Earthquake rupture dynamics frozen in exhumed ancient faults. Nature 436 (7053), 1009–1012. https://doi.org/10.1038/nature03910.

Di Toro, G., Pennacchioni, G., Nielsen, S., 2009. Pseudotachylytes and earthquake source mechanics. In: Fukuyama, Eiichi (Ed.), Fault-Zone Properties and Earthquake Rupture Dynamics, International Geophysics, 94, pp. 87–133. https://doi.org/10.1016/S0074-6142(08)00005-3.

Fagereng, Å., Sibson, R.H., 2010. Mélange rheology and seismic style. Geology 38 (8), 751–754. https://doi.org/10.1130/G30868.1.

Fagereng, Å., Remitti, F., Sibson, R.H., 2010. Shear veins observed within anisotropic fabric at high angles to the maximum compressive stress. Nat. Geosci. 3 (7), 482–485. https://doi.org/10.1038/ngeo898.

Faulkner, D.R., Sanchez-Roa, C., Boulton, C., Den Hartog, S.A.M., 2018. Pore fluid pressure development in compacting fault gouge in theory, experiments, and nature. J. Geophys. Res. Solid Earth 123 (1), 226–241. https://doi.org/10.1002/2017JB015130.

Ferri, F., Di Toro, G., Hirose, T., Han, R., Noda, H., Shimamoto, T., Quaresimin, M., de Rossi, N., 2011. Low-to high-velocity frictional properties of the clay-rich gouges from the slipping zone of the 1963 Vaiont slide, northern Italy. J. Geophys. Res. Solid Earth 116 (B9). https://doi.org/10.1029/2011JB008338.

Festa, A., Pini, G.A., Dilek, Y., Codegone, G., 2010. Mélanges and mélange-forming processes: a historical overview and new concepts. Int. Geol. Rev. 52 (10–12), 1040–1105. https://doi.org/10.1080/00206810903557704.

Hekinian, R., Bideau, D., Cannat, M., Francheteau, J., Hébert, R., 1992. Volcanic activity and crust-mantle exposure in the ultrafast Garrett transform fault near 13°28′S in the Pacific. Earth Planet Sci. Lett. 108 (4), 259–275. https://doi.org/10.1016/0012-821X(92)90027-S.

Hirose, T., Bystricky, M., 2007. Extreme dynamic weakening of faults during dehydration by coseismic shear heating. Geophys. Res. Lett. 34, L14311.

Hirose, T., Shimamoto, T., 2005. Growth of molten zone as a mechanism of slip weakening of simulated faults in gabbro during frictional melting. J. Geophys. Res. Solid Earth 110 (B5). https://doi.org/10.1029/2004JB003207.

Huber, M.L., et al., 2009. New international formulation for the viscosity of H_2O. J. Phys. Chem. Ref. Data 38, 101–125.

Hung, C.C., Kuo, L.W., Spagnuolo, E., Wang, C.C., Di Toro, G., Wu, W.J., Dong, J.J., Lin, W., Sheu, H.S., Yeh, E.C., Hsieh, P.S., 2019. Grain fragmentation and frictional melting during initial experimental deformation and implications for seismic slip at shallow depths. J. Geophys. Res. Solid Earth 124 (11), 11150–11169. https://doi.org/10.1029/2019JB017905.

Hyndman, R.D., Peacock, S.M., 2003. Serpentinization of the forearc mantle. Earth Planet Sci. Lett. 212 (3–4), 417–432. https://doi.org/10.1016/S0012-821X(03)00263-2.

Kimura, G., Yamaguchi, A., Hojo, M., Kitamura, Y., Kameda, J., Ujiie, K., Hamada, Y., Hamahashi, M., Hina, S., 2012. Tectonic mélange as fault rock of subduction plate boundary. Tectonophysics 568, 25–38. https://doi.org/10.1016/j.tecto.2011.08.025.

Kitajima, H., Chester, J.S., Chester, F.M., Shimamoto, T., 2010. High-speed friction of disaggregated ultracataclasite in rotary shear: characterization of frictional heating, mechanical behavior, and microstructure evolution. J. Geophys. Res. 115 (B8), B08408.

Kohli, A.H., Goldsby, D.L., Hirth, G., Tullis, T., 2011. Flash weakening of serpentinite at near-seismic slip rates. J. Geophys. Res. Solid Earth 116 (B3). https://doi.org/10.1029/2010JB007833.

Kuo, L.W., Song, S.R., Huang, L., Yeh, E.C., Chen, H.F., 2011. Temperature estimates of coseismic heating in clay-rich fault gouges, the Chelungpu fault zones, Taiwan. Tectonophysics 502 (3–4), 315–327. https://doi.org/10.1016/j.tecto.2011.02.001.

Kuo, L.-W., Hsiao, H.-C., Song, S.-R., Sheu, H.-S., Suppe, J., 2014. Coseismic thickness of principal slip zone from the Taiwan Chelungpu fault Drilling Project-A (TCDP-A) and correlated fracture energy. Tectonophysics 619–620, 29–35.

Kuo, L.W., Wu, W.J., Kuo, C.W., Smith, S.A., Lin, W.T., Wu, W.H., Huang, Y.H., 2021. Frictional strength and fluidization of water-saturated kaolinite gouges at seismic slip velocities. J. Struct. Geol. 150, 104419. https://doi.org/10.1016/j.jsg.2021.104419.

Kuo, L.W., Hung, C.C., Li, H., Aretusini, S., Chen, J., Di Toro, G., Spagnuolo, E., Di Felice, F., Wang, H., Si, J., Sheu, H.S., 2022a. Frictional properties of the Longmen Shan fault belt gouges from WFSD-3 and implications for earthquake rupture propagation. J. Geophys. Res. Solid Earth 127 (5). https://doi.org/10.1029/2022JB024081.

Kuo, L.-W., Sone, H., Luzin, V., Yeh, E.-C., Hsu, Y.-J., Tan, E., 2022b. Gouge fabrics reset by thermal pressurization record stress on faults after earthquakes. Geology. https://doi.org/10.1130/G50217.1.

Lachenbruch, A.H., 1980. Frictional heating, fluid pressure, and the resistance to fault motion. J. Geophys. Res. Solid Earth 85 (B11), 6097–6112. https://doi.org/10.1029/JB085iB11p06097.

Lin, A., Takano, S., Hirono, T., Kanagawa, K., 2013. Coseismic dehydration of serpentinite: evidence from high-velocity friction experiments. Chem. Geol. 344, 50–62. https://doi.org/10.1016/j.chemgeo.2013.02.013.

Llana-Fúnez, S., Brodie, K.H., Rutter, E.H., Arkwright, J.C., 2007. Experimental dehydration kinetics of serpentinite using pore volumometry. J. Metamorph. Geol. 25, 423–438.

Maurer, J., Johnson, K., 2014. Fault coupling and potential for earthquakes on the creeping section of the central San Andreas fault. J. Geophys. Res. Solid Earth 119 (5), 4414–4428. https://doi.org/10.1002/2013JB010741.

Melekhova, E., Schmidt, M.W., Ulmer, P., Guggenbühl, E., 2006. The reaction talc + forsterite = enstatite + H2O revisited: application of conventional and novel experimental techniques and derivation of revised thermodynamic properties. Am. Mineral. 91 (7), 1081–1088. https://doi.org/10.2138/am.2006.2065.

Meneghini, F., Marroni, M., Moore, J.C., Pandolfi, L., Rowe, C.D., 2009. The processes of underthrusting and underplating in the geologic record: structural diversity between the Franciscan Complex (California), the Kodiak Complex (Alaska) and the Internal Ligurian Units (Italy). Geol. J. 44 (2), 126–152. https://doi.org/10.1002/gj.1144.

Moore, D.E., Rymer, M.J., 2012. Correlation of clayey gouge in a surface exposure of serpentinite in the San Andreas Fault with gouge from the San Andreas Fault Observatory at Depth (SAFOD). J. Struct. Geol. 38, 51–60. https://doi.org/10.1016/j.jsg.2011.11.014.

Nguyen, T.T., Kuo, L.-W., Kong, Q.-E., Kuo, C.-W., Dong, J.-J., Brown, D., Wang, H., Kuo, S.-T., Li, H., Si, J., 2024. Fluid drainage leads to thermal decomposition of wet gouge during experimental seismic slip. Geophys. Res. Lett. 51 (18). https://doi.org/10.1029/2023GL106879.

Osako, M., et al., 2010. Thermal diffusivity, thermal conductivity, and heat capacity of serpentine (antigorite) under high pressure. Phys. Earth Planet. Inter. 183, 229–233.

Peacock, S.M., Christensen, N.I., Bostock, M.G., Audet, P., 2011. High pore pressures and porosity at 35 km depth in the Cascadia subduction zone. Geology 39, 471–474.

Poliakov, A.N., Dmowska, R., Rice, J.R., 2002. Dynamic shear rupture interactions with fault bends and off-axis secondary faulting. J. Geophys. Res. Solid Earth 107 (B11), ESE–6. https://doi.org/10.1029/2001JB000572.

Proctor, B.P., Mitchell, T.M., Hirth, G., Goldsby, D., Zorzi, F., Platt, J.D., Di Toro, G., 2014. Dynamic weakening of serpentinite gouges and bare surfaces at seismic slip rates. J. Geophys. Res. Solid Earth 119 (11), 8107–8131. https://doi.org/10.1002/2014JB011057.

Rempel, A.W., Rice, J.R., 2006. Thermal pressurization and onset of melting in fault zones. J. Geophys. Res. Solid Earth 111 (B9). https://doi.org/10.1029/2006JB004314.

Reynard, B., 2013. Serpentine in active subduction zones. Lithos 178, 171–185. https://doi.org/10.1016/j.lithos.2012.10.012.

Rice, J.R., 2006. Heating and weakening of faults during earthquake slip. J. Geophys. Res. Solid Earth 111 (B5). https://doi.org/10.1029/2005JB004006.

Seipold, U., Schilling, F.R., 2003. Heat transport in serpentinites. Tectonophysics 370, 147–162.

Smith, S.A., Tarling, M.S., Negrini, M., Allan, S.J., Ellis, S., Palmer, M., Viti, C., Reid, M. R., 2024. Slip and stress in block-in-matrix shear zones: 1. microstructure and mineralogy of a serpentine-filled dilational jog. J. Struct. Geol. 186, 105220. https://doi.org/10.1016/j.jsg.2024.105220.

Steinike, U., Tkácová, K., 2000. Mechanochemistry of solids—real structure and reactivity. J. Mater. Synth. Process. 8 (3–4), 197–203. https://doi.org/10.1023/A:1011364110355.

Tarling, M.S., Smith, S.A., Viti, C., Scott, J.M., 2018. Dynamic earthquake rupture preserved in a creeping serpentinite shear zone. Nat. Commun. 9 (1), 3552. https://doi.org/10.1038/s41467-018-05965-0.

Tarling, M.S., Smith, S.A., Scott, J.M., Rooney, J.S., Viti, C., Gordon, K.C., 2019a. The internal structure and composition of a plate-boundary-scale serpentinite shear zone: the Livingstone Fault, New Zealand. Solid Earth 10 (4), 1025–1047. https://doi.org/10.5194/se-10-1025-2019.

Tarling, M.S., Smith, S.A.F., Scott, J.M., 2019b. Fluid overpressure from chemical reactions in serpentinite within the source region of deep episodic tremor. Nat. Geosci. 12, 1034–1042. https://doi.org/10.1038/s41561-019-0470-z.

Tarling, M.S., Smith, S.A.F., Negrini, M., et al., 2022. An evolutionary model and classification scheme for nephrite jade based on veining, fabric development, and the role of dissolution–precipitation. Sci. Rep. 12, 7823. https://doi.org/10.1038/s41598-022-11560-7.

Tesei, T., Harbord, C.W.A., De Paola, N., Collettini, C., Viti, C., 2018. Friction of mineralogically controlled serpentinites and implications for fault weakness. J. Geophys. Res. Solid Earth 123 (8), 6976–6991. https://doi.org/10.1029/2018JB016058.

Tisato, N., Di Toro, G., De Rossi, N., Quaresimin, M., Candela, T., 2012. Experimental investigation of flash weakening in limestone. J. Struct. Geol. 38, 183–199. https://doi.org/10.1016/j.jsg.2011.11.017.

Ujiie, K., Tsutsumi, A., Kemeda, J., 2011. Reproduction of thermal pressurization and fluidization of clay-rich fault gouges by high-velocity friction experiments and implications for seismic slip in natural faults. In: Fagereng, Å., Toy, V.G., Rowland, J. V. (Eds.), Geology of the Earthquake Source: a Volume in Honour of Rick Sibson, 359. Geological Society, London, Special Publications, pp. 267–285.

Ujiie, K., Saishu, H., Fagereng, Å., Nishiyama, N., Otsubo, M., Masuyama, H., Kagi, H., 2018. An explanation of episodic tremor and slow slip constrained by crack-seal veins and viscous shear in subduction mélange. Geophys. Res. Lett. 45 (11), 5371–5379. https://doi.org/10.1029/2018GL078374.

Violay, M., Nielsen, S., Gibert, B., Spagnuolo, E., Cavallo, A., Azais, P., Vinciguerra, S., Di Toro, G., 2014. Effect of water on the frictional behavior of cohesive rocks during earthquakes. Geology 42 (1), 27–30. https://doi.org/10.1130/G34916.1.

Viti, C., 2010. Serpentine minerals discrimination by thermal analysis. Am. Mineral. 95, 631–638.

Viti, C., Hirose, T., 2009. Dehydration reactions and micro/nanostructures in experimentally-deformed serpentinites. Contrib. Mineral. Petrol. 157, 327–338. https://doi.org/10.1007/s00410-008-0337-6.

Viti, C., Hirose, T., 2010. Thermal decomposition of serpentine during coseismic faulting: nanostructures and mineral reactions. J. Struct. Geol. 32 (10), 1476–1484. https://doi.org/10.1016/j.jsg.2010.09.009.

Viti, C., Collettini, C., Tesei, T., Tarling, M.S., Smith, S.A., 2018. Deformation processes, textural evolution and weakening in retrograde serpentinites. Minerals 8 (6), 241. https://doi.org/10.3390/min8060241.

Wagner, W., Pruß, A., 2002. The IAPWS formulation 1995 for the thermodynamic properties of ordinary water substance for general and scientific use. J. Phys. Chem. Ref. Data 31, 387–535.

Weatherley, D.K., Henley, R.W., 2013. Flash vaporization during earthquakes evidenced by gold deposits. Nat. Geosci. 6 (4), 294–298. https://doi.org/10.1038/ngeo1759.

Wibberley, C.A., Shimamoto, T., 2005. Earthquake slip weakening and asperities explained by thermal pressurization. Nature 436 (7051), 689–692. https://doi.org/10.1038/nature03901.

Wu, W.J., Kuo, L.W., Ku, C.S., Chiang, C.Y., Sheu, H.S., Aprilniadi, T.D., Dong, J.J., 2020. Mixed-mode formation of amorphous materials in the creeping zone of the Chihshang Fault, Taiwan, and implications for deformation style. J. Geophys. Res. Solid Earth 125 (6). https://doi.org/10.1029/2020JB019862.

Xu, Y., et al., 2004. Thermal diffusivity and conductivity of olivine, wadsleyite, and ringwoodite to 20 GPa and 1373 K. Phys. Earth Planet. Inter. 143, 321–336.

Yao, L., Ma, S., Di Toro, G., 2023. Coseismic fault sealing and fluid pressurization during earthquakes. Nat. Commun. 14 (1), 1136. https://doi.org/10.1038/s41467-023-36839-9.